



HAL
open science

Dry lubrication of ferritic stainless steel functionalised with crystalline aggregates of hexadecylphosphonic acid

Pierre-Henri Cornuault, Jean-Marie Melot, Xavier Roizard, Fabrice Lallemand

► To cite this version:

Pierre-Henri Cornuault, Jean-Marie Melot, Xavier Roizard, Fabrice Lallemand. Dry lubrication of ferritic stainless steel functionalised with crystalline aggregates of hexadecylphosphonic acid. *Tribology International*, 2020, 145, pp.106139. 10.1016/j.triboint.2019.106139 . hal-02735603

HAL Id: hal-02735603

<https://hal.science/hal-02735603>

Submitted on 7 Mar 2022

HAL is a multi-disciplinary open access archive for the deposit and dissemination of scientific research documents, whether they are published or not. The documents may come from teaching and research institutions in France or abroad, or from public or private research centers.

L'archive ouverte pluridisciplinaire **HAL**, est destinée au dépôt et à la diffusion de documents scientifiques de niveau recherche, publiés ou non, émanant des établissements d'enseignement et de recherche français ou étrangers, des laboratoires publics ou privés.



Distributed under a Creative Commons Attribution - NonCommercial 4.0 International License

Dry lubrication of ferritic stainless steel functionalised with crystalline aggregates of hexadecylphosphonic acid

Pierre-Henri Cornuault ^{1*}, Jean-Marie Melot ², Xavier Roizard ¹, Fabrice Lallemand ^{2,3}

¹ Femto-ST Institute – Department of Applied Mechanics, UBFC, CNRS UMR 6174, Besançon, France

² UTINAM Institute, UBFC, CNRS UMR 6213, Besançon, France

³ AFULudine Inc., Dole, France; www.afuludine.com

* Corresponding author: pierre-henri.cornuault@ens2m.fr
+ 33(0)381402854

Abstract

This paper demonstrates the excellent tribological behaviour afforded by a new functionalisation technique based on the combination of chemisorption and physisorption of self-assembled hexadecylphosphonic acid for application in metal forming. Surface functionalisation of an X2TiCrNb18 ferritic stainless steel with this technique led to the growth of aggregates on the surface. Detailed analysis showed that crystalline aggregates were physisorbed on a chemisorbed molecular layer. Ball-on-plate linear reciprocating sliding tests were performed under high maximal contact pressures in the 0.5–1.1 GPa range using a 100Cr6 counterpart. Results revealed exceptional low-friction and low-wear afforded by a tribofilm originating from aggregates shearing. The tribofilm built up very quickly and presented the interesting feature of reducing the friction coefficient as the contact pressure increased.

Keywords

alkylphosphonic acid; dry lubrication; tribofilm; surface functionalisation

1. Introduction

Stainless steels are metallic alloys widely used in numerous everyday-life and industrial applications. Among them, a large amount of sheet or shell shaped components are formed through stamping, embossing or rolling operations. Since high mechanical stresses are transmitted to the tool/material interface to reach the required plastic deformation to form stainless steel products, lubricants are necessary for two main reasons. First: to ensure surface integrity of both the tool and the component: this issue is of major concern regarding stainless steels forming operations since well-known adhesion phenomena easily occur in the absence of lubricant^{1–3}. Second: to minimize friction forces at the tool/material interface, in the perspective of costs and energy consumption reduction.

For many years, mineral-based lubricants containing friction modifiers and extreme pressure additives have been widely employed in metal forming and they are still known to be the most efficient ones. Indeed, these compounds tribochemically react with the metal surface to form highly efficient tribofilms whose shearing ensures the accommodation of the surfaces⁴. However, lubricant additives are chlorine, sulphur and/or phosphorous compounds that are nowadays facing to environmental restrictions due their toxicity and poor biodegradability. The development of efficient “green-

lubricants” dedicated to metal forming is thus a major challenge. “Bio-lubricants” based on vegetable oils aroused interest in the last years but their potential use in metal forming is confronted to their low oxidative stability, poor low-temperature rheological behaviour, and the necessity to incorporate nanoparticles of metal oxides to improve their efficiency⁵⁻⁷. Moreover and from a wider prospective, the use of lubricants in liquid form infers an additional issue since they have to be eliminated after metal forming operations in most cases. Subsequent cleaning operations have thus to be performed to complete further manufacturing operations (welding, soldering, polishing...), leading to time-consumption and additional costs.

Functionalisation of metal sheets with organic molecular species offers a convincing option to circumvent the above-mentioned drawbacks of classical lubricants. This leads to the chemisorption on the metal surface of an organised molecular layer, so-called self-assembled monolayer (SAM), through the simple immersion of the metal into a weakly concentrated solution of reactive molecules dissolved in a solvent. Grafting of SAM has proven to be a powerful method to control surface properties, including frictional ones⁸, due to its simplicity, adaptability, and reproducibility⁹. Improvement of the tribological behaviour of various metallic surfaces was reported by grafting highly studied SAMs such as organothiols or organosilanes¹⁰⁻¹². Notwithstanding, alkylphosphonic acids have naturally aroused much more interest in the past few years due to their lower toxicity and their ability to form strong O–P bonds on surface metal oxides¹³. Grafting of alkylphosphonic acids and subsequent improvement of tribological properties were successfully achieved on copper¹⁴⁻¹⁶, aluminium oxides^{17,18}, titanium alloys¹⁹, Ti incorporated carbon coatings²⁰, TiO₂-coated galvanized steel²¹, and stainless steel²².

However, almost all studies were focused on the behaviour of well-organized SAMs whose realisation implies complex surface preparation and the removal through ultrasonication of physisorbed species that were not chemically adsorbed on the surface. Such additional treatments are hardly achievable at the industrial scale in the framework of metal forming. A few years ago, the authors reported exceptional low-friction and low-wear properties exhibited by dodecylphosphonic acids grafted on copper, due to the presence of physisorbed molecular clusters on the surface¹⁶. This finding led to a new functionalisation technique avoiding surface post-treatment and deliberately promoting the existence of physisorbed molecular aggregates on the original chemisorbed monolayer. Recently, the new functionalisation route was patented²³ and applied in stamping operations realised on stainless steel in industrial framework²⁴. The performance of a lubricant for stamping operations, in terms of drawability, is usually quantified by the Limiting Drawing Ratio (LDR) defined as the ratio of the maximum blank diameter to the punch diameter that can be drawn successfully without failure²⁵. The drawability increases with increasing LDR values. Whereas oils traditionally used in metal forming (chlorinated or not) leads to LDR ranging from 1.98 to 2.25, the new functionalisation technique was found to achieve LDR ranging from 2.24 to 2.35²⁴. This lubricating method therefore has the double advantage to provide similar or even better performance than the best conventional oils while avoiding cleaning operations. Nonetheless, both the characterisation of this advanced functionalisation and the tribological mechanisms involved have not been published yet.

The present paper consequently addresses those limitations. This study focuses on the tribological behaviour of hexadecylphosphonic acids adsorbed on a ferritic stainless steel. The growing of crystalline aggregates originating from clustered hexadecylphosphonic acids is demonstrated and characterised for the first time. A fully instrumented tribometer is used to perform tests in relevant contact pressures with respect to metal forming operations. The tribological behaviour afforded by the new functionalisation technique is compared with this of stainless steel substrate functionalised (or not) with a classical monolayer of the same molecule. An approach coupling friction force measurements and surface modification characterisation is conducted. It reveals improved tribological properties that are induced by the presence of crystalline aggregates, building up and then destruction of a protecting tribofilm, and the transient frictional behaviour of this film.

2. Materials and Methods

2.1. Materials

The present study focuses on the functionalization of an X2TiCrNb18 ferritic stainless steel (AISI 441, 1.4509). The trade name K41 will be used thereafter for the sake of clarity. K41 was used as received, i.e. in the annealed state and without additional polishing operation, and in the form of 15×15 mm² plates of 1.25 mm thickness. The tribological behaviour of functionalised K41 plates were further considered when rubbing against a 100Cr6 steel ball counterpart. Mechanical properties and surface roughness parameters of the raw samples are displayed in Table 1.

Table 1:

Sample	Young's Modulus * [GPa]	Poisson's ratio *	Hardness § [GPa]	Yield strength * [MPa]	Sa # [μm]	Ssk #	Sku #
K41 plate	220	0.29	1.62 ± 0.03	310	2.88 ± 0.25	-0.08 ± 0.12	4.76 ± 0.65
100Cr6 ball	210	0.3	8.12 ± 0.14	750	0.21 ± 0.02	0.29 ± 0.27	4.01 ± 0.53

* Data provided by the suppliers.

§ Data originate from 5 measurements using a Vickers hardness tester with a 5 kg load.

Results from the measurement of 5 surfaces (0.5×0.5 mm² for the plates and 0.2×0.2 mm² for the balls) using a variable focus optical microscope InfiniteFocus from Alicona Imaging GmbH.

Table 1: Mechanical properties and surface roughness parameters of the raw samples.

From Table 1, it is worth mentioning that the distribution of the peaks for both plates and balls is symmetric (Ssk close to 0) and is slightly more peaked than a Gaussian distribution since Sku exceeds 3. Moreover, balls are more than 10 times smoother and 5 times harder than plates.

2.2. Synthesis of hexadecylphosphonic acid

Finely powdered hexadecylphosphonic $\text{CH}_3(\text{CH}_2)_{15}\text{PO}(\text{OH})_2$ was obtained through a reproducible synthesis of this molecule on a 0.2–0.5 kg scale. All reagents were purchased from ALFA AESAR and used as received.

First, 1 mol of 1-bromohexadecane was heated to 190–200°C with stirring and excess of triethylphosphite (1.3 mol) was added dropwise during 2.5 h. The formed bromoethane was concomitantly distilled (boiling point = 35–40°C). Heating was maintained for 1 h, and then all the volatiles (excess triethyl phosphite and some diethyl ethylphosphonate) were distilled under reduced pressure (90–100°C, 20 mm Hg). Crude diethyl hexadecylphosphonate was obtained in essential quantitative yield (purity > 85% estimated by ¹H NMR). The product generally crystallized at room temperature to a thick waxy material.

Second, the former phosphonate was boiled for 16 h with commercial 70% aqueous methanesulfonic acid to obtain a dark thick mixture: 2.5 mol of water per mole of phosphonate were needed. After cooling to 30°, technical acetone was added under vigorous stirring, which precipitated

hexadecylphosphonic acid. After filtration and thorough washing with acetone, crystals of hexadecylphosphonic acid (CRY) were finally obtained as a fluffy white powder of high degree of purity (global yield, 2 steps: 65-70%).

2.3. Surface functionalisation and characterization

Nine K41 plates were first ultrasonically cleaned in absolute ethanol during 5 min and then dried at ambient air. Two of them were stored as reference samples. They will be denominated K41 in the followings.

Six of the 7 remaining plates were dipped during 6 h in a glass-vessel containing 15 mL of a solution (SOL) obtained by dilution of CRY in absolute ethanol, resulting in a 2×10^{-2} M concentrated solution of hexadecylphosphonic acid dissolved in the solvent. This operation traditionally results in the chemisorption of the molecules on the substrate. Two distinctive functionalisation routes were achieved depending on the technique used to remove the plate from the SOL and to dry it. The goal of the first technique was to form a chemisorbed layer of grafted hexadecylphosphonic acids on the plate and to avoid the presence of physisorbed molecules. To this end, 2 plates were heavily rinsed with ethanol during 2 min just after their removal from the SOL and were then dried at ambient air in vertical position. The functionalised plates will be called SAM thereafter, in relation to the foreseen formation of self-assembled monolayers on the substrate. Conversely, the second technique consisted in maintaining the sample in horizontal position just after its removal from the SOL and without cleaning operation in order to promote the additional aggregation of physisorbed species onto the chemisorbed layer during the solvent evaporation. The present study mainly focuses on the 4 plates functionalised through this innovative technique. They will be called AGG in the followings.

All AGG and SAM samples were stored at ambient air during 1 week prior experiments to ensure total evaporation of the solvent. One of each AGG and SAM samples were analysed by Attenuated Total Reflectance Fourier Transform InfraRed spectroscopy (ATR-FTIR) while the 4 others (3 AGG and 1 SAM) were dedicated to friction testing (cf. section 2.4). Prior to ATR-FTIR analyses, XRD measurements were performed on the AGG sample and on one K41 as reference.

ATR-FTIR analyses were performed with a 2 cm^{-1} resolution using a Nicolet Nexus spectrometer equipped with a ZnSe internal reflectance element. XRD measurements were carried out with a Bruker D8 Advance diffractometer equipped with a Cu-K α radiation source operated at 40 kV and 40 mA and using a step-scan mode of 0.01° between $2\theta = 10$ to 90° . A pellet of compacted CRY was also analysed by both ATR-FTIR and XRD as a reference.

The last remaining K41 plate was used to observe the evolution of the surface during the evaporation stage according to the second technique (leading to AGG). To this end, a video caption of the plate surface was recorded at x50 magnification with a KEYENCE VHX-6000 numerical microscope just after the deposition of $5 \mu\text{L}$ of SOL onto the plate and until the end of the solvent evaporation.

2.4. Friction tests

The tribological behaviour of the functionalised and un-functionalised stainless steel samples (K41, SAM, and AGG) were tested in dry sliding condition against a 5 mm diameter 100Cr6 steel ball counterpart. Before experiments, balls were ultrasonically cleaned in absolute ethanol during 10 min and then air-dried. Ball-on-plate friction tests were then performed at $24 \pm 3^\circ\text{C}$ using a custom-made tribometer achieving reciprocating linear motion with a ± 1 mm displacement stroke at 1 Hz. Backward-and-forward friction cycles were carried out with a fixed $4 \text{ mm}\cdot\text{s}^{-1}$ sliding speed. A fixed normal force (F_N) was applied throughout the test using dead loads. Depending on the test, F_N ranged

from 0.25 to 3 N leading to mean and maximal Hertzian contact pressures (P_{mean} and P_{max}) in the range of 317–725 MPa and 475–1,088 MPa, respectively, calculated with:

$$P_{\text{max}} = \frac{3}{2} P_{\text{mean}} = \frac{3}{2} \left(\frac{16 F_N E^*}{9 \pi^3 R^2} \right)^{1/3} \quad (1)$$

where $R = 2.5$ mm is the ball radius, and $E^* = 118$ GPa is the reduced modulus of the contact calculated with the elastic properties of the materials presented in Table 1.

In the framework of a first test campaign, 250 friction cycles were performed on the three ball/plate configurations studied, i.e. involving AGG, SAM, and K41 samples. Friction tests realised on AGG were achieved under $P_{\text{mean}} = 317, 399, 503, 633$ and 725 MPa, and friction tests on K41 and SAM were achieved under $P_{\text{mean}} = 317, 503$ and 725 MPa. For each contact pressure applied, 6 tests on AGG and 3 tests on both K41 and SAM samples were performed for reproducibility. The tribological behaviour of AGG during the first friction cycles was further investigated through a second test campaign. To this end, tests under $P_{\text{mean}} = 317, 503$ and 725 MPa were conducted up to 45 friction cycles on AGG and on K41 as a reference. In addition, other tests carried out on AGG under $P_{\text{mean}} = 503$ MPa were stopped after 1, 3, 11 and 71 friction cycles. All tests performed within this second test campaign were tripled for reproducibility.

Throughout each test, the relative displacement of the ball (h) and the friction force (F_T) were measured thanks to LVDT and piezoelectric sensors, respectively. Both signals were recorded with a 512 Hz sampling frequency. Data post-processing was performed in order to plot the local friction coefficient (F_T/F_N) versus h for each friction cycle. Finally, the mean friction coefficient (μ) related to an overall friction cycle was calculated from an energetic point of view as follows:

$$\mu = \frac{\int |F_T| dh}{2 h_0 F_N} \quad (2)$$

where h_0 is the distance between the two positions on the friction track where $F_T = 0$ (very close to 2 mm). More details about this method can be found in²⁶.

2.5. Friction tracks characterization

Surface topography characterization of the friction tracks were performed using a variable focus optical microscope InfiniteFocus from Alicona Imaging GmbH. Data were then post-processed with a specific custom-made image treatment software allowing for 3D surface topography visualisation and roughness profiles plotting. Samples were then gold metallised to analyse the friction tracks by Scanning Electron Microscopy (SEM). SEM imaging was performed using a high-resolution TESCAN SEM-FEG MIRA3 operated at 5 kV.

3. Results and discussions

3.1. Growth of crystalline aggregates of hexadecylphosphonic acid

The growth of aggregates of hexadecylphosphonic acids on the same zone of the surface of a K41 sample at different times is displayed in Figure 1. From the deposition of the SOL droplet on the surface at $t = 0$ to $t = 66$ s, no visible modification of the K41 surface was observed. Nonetheless, small clusters with dimensions in the order of a few hundreds of micrometres were meanwhile detected in the SOL. They quickly moved in the liquid phase according to a Brownian motion allowing to assume that hexadecylphosphonic molecules were only partially dissolved in the solvent when the SOL was prepared. Through the gradual decrease of the overall SOL volume induced by solvent evaporation, some molecules' aggregates appeared on the surface as grey-black patches, as

highlighted in Figure 1 at $t = 72$ s. While some aggregates originated from the deposition of the free-to-move clusters present in the SOL, most of them seemed emanating from a germination process on the surface. Fast growing of the aggregates into the SOL then occurred during the ten following seconds (cf Figure 1 at $t = 76$ and 79 s). Thereafter, the whitening of the surface observed from $t = 79$ to 90 s indicates the end of the evaporation step. The solvent agglomerated close to aggregates leading to their further growing due to a local increase of the molecules concentration. At $t = 96$ s, solvent evaporation seemed apparently completed. Interestingly, a discontinuous brown film finally appeared on the surface between aggregates.

Figure 1:

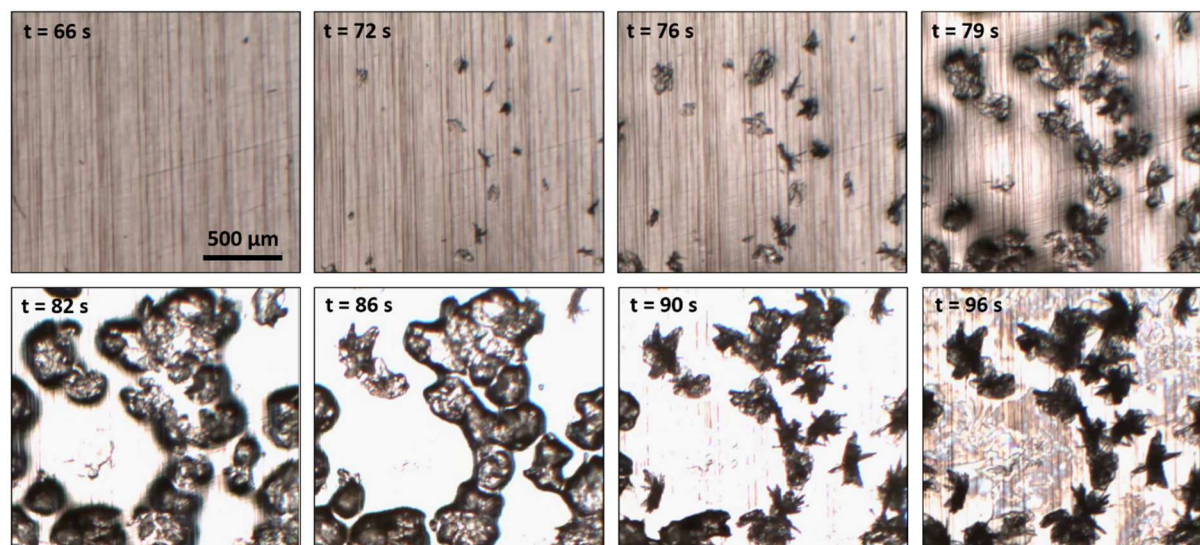


Figure 1: Microscope observations at different times of the growth of hexadecylphosphonic acid aggregates on the same zone of a K41 surface. A $5 \mu\text{L}$ droplet of 2×10^{-2} M of $\text{CH}_3(\text{CH}_2)_{15}\text{PO}(\text{OH})_2$ molecules diluted in ethanol was deposited on the K41 surface at $t = 0$.

Since Figure 1 helps to understand the main mechanisms of hexadecylphosphonic acid aggregation on the substrate, it is worth mentioning that the operating conditions of this aggregation are somewhat different from those related to the realisation of AGG samples. Indeed, longer evaporation times (close to 3 min) were qualitatively observed for AGG due to both higher initial SOL volume and the absence of microscope lighting which may cause heating. Nonetheless, SEM observations of an AGG sample displayed in Figure 2 show similar features and allow to clarify the nature of the aggregates and the brown film previously described. The steel sample is covered by large but fine platelets that are several hundreds of micrometres long and a few micrometres thick. They are mainly arranged parallel to the surface **and they only partially cover the surface (dark zones in Figure 2a)**. Notwithstanding, some of them are clustered into three-dimensional structures (cf Figures 2b and 2c) where platelets tend to be oriented perpendicularly to the surface, recalling the black patches observed in Figure 1. Occasionally, these clusters also comprise needle-shaped structures, as depicted in Figure 2d. Both platelets and needles exhibit geometrical features which strongly support a crystalline nature. As compared with Figure 1, it is assumed that the lower density of three-dimensional clusters and the higher density of platelets spread on the surface originate from the above-mentioned differences in the evaporation process.

Figure 2:

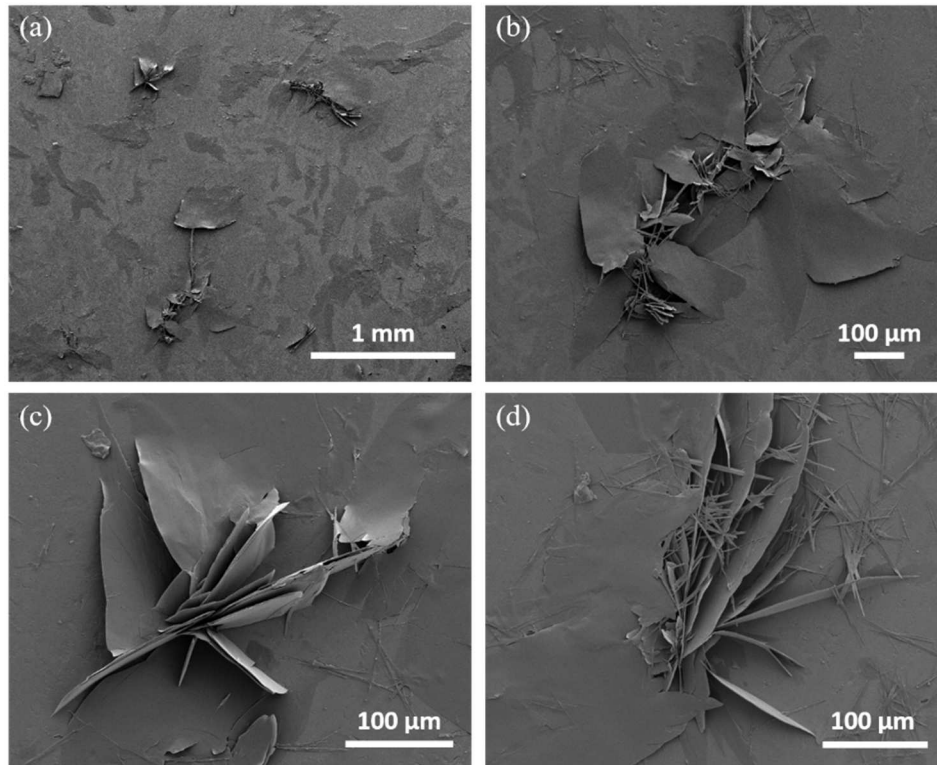


Figure 2: SEM observations of an AGG sample, i.e. prepared according to the second functionalisation protocol involving the natural evaporation of the SOL on the substrate.

Figure 3a displays the surface topography obtained on AGG samples after functionalisation associated with a microscopic observation of the same zone. The highest peaks of the surface match the position of the three-dimensional clusters. Although the highest clusters can reach up to approximately 30 μm **in reference to the mean height of the whole surface analysed**, most of them do not exceed 15 μm. Nonetheless, it seems that crystalline platelets oriented parallel to the surface do not increase to a large extent the original roughness of the substrate. Indeed, $S_a = 4.92 \pm 0.53 \mu\text{m}$ on AGG but it reached $2.95 \pm 0.33 \mu\text{m}$ without taking into account the clusters in the analyses, that is close to the K41 roughness. Consistently, S_{sk} increased to reach 0.81 ± 0.63 on AGG due to the presence of peaked clusters on the surface.

The thickness of individual platelets oriented parallel to the surface was analysed through local topographic analyses where peaked clusters are absent and the substrate is easily observed. After segmentation of the areas related to the platelet on the one hand and of the substrate on the other hand, the shift between the maximum of the two corresponding peaks' height distribution was measured. As a typical example of numerous analyses performed in **this** way, Figures 3b and 3c confirm the thinness of the individual platelets oriented parallel to the surface. Their thickness typically ranges from 0.1 to 0.4 μm with a mean value of 262 nm. Stacking of several platelets also occurs, resulting in several micrometres thick patches.

Figure 3:

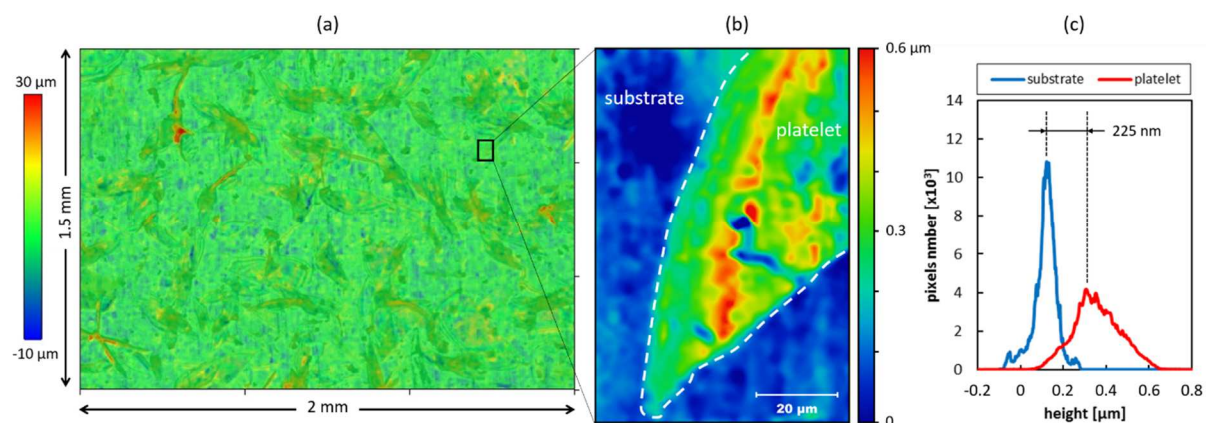


Figure 3: (a) Topography of AGG samples after functionalization: Optical microscopy observation (grey scale - 25% weighted) overlays the topography (colour scale - 75% weighted) of the same zone. (b) Topographic analysis focused on the corner of a single crystalline platelet oriented parallel to the surface. (c) Peaks' height distribution referring to the substrate (blue curve) and the platelet (red curve) appearing in (b). The shift between the two distributions indicates the platelet thickness.

The XRD pattern of AGG displayed in Figure 4a confirms the presence of crystalline species on the surface. Obviously, peaks at $2\theta = 44^\circ$, 65° and 82° refer to the underlying K41 body-centred cubic structure, but the numerous peaks located at 2θ values lower than 30° are in agreement with the presence of crystalline organic compounds and consistent with XRD patterns recorded on lamellar octadecylphosphonic acid²⁷. In this 2θ range, the AGG spectrum is similar to that of CRY although a shift of the peaks occurs. This suggests a slight modification of the crystallographic structure after growing through the solvent evaporation process, as compared with the original crystal of hexadecylphosphonic acid. Unfortunately, to our knowledge, the absence of registered pattern of this crystal in XRD databases makes difficult more in-depth investigation of this structural difference.

Figure 4:

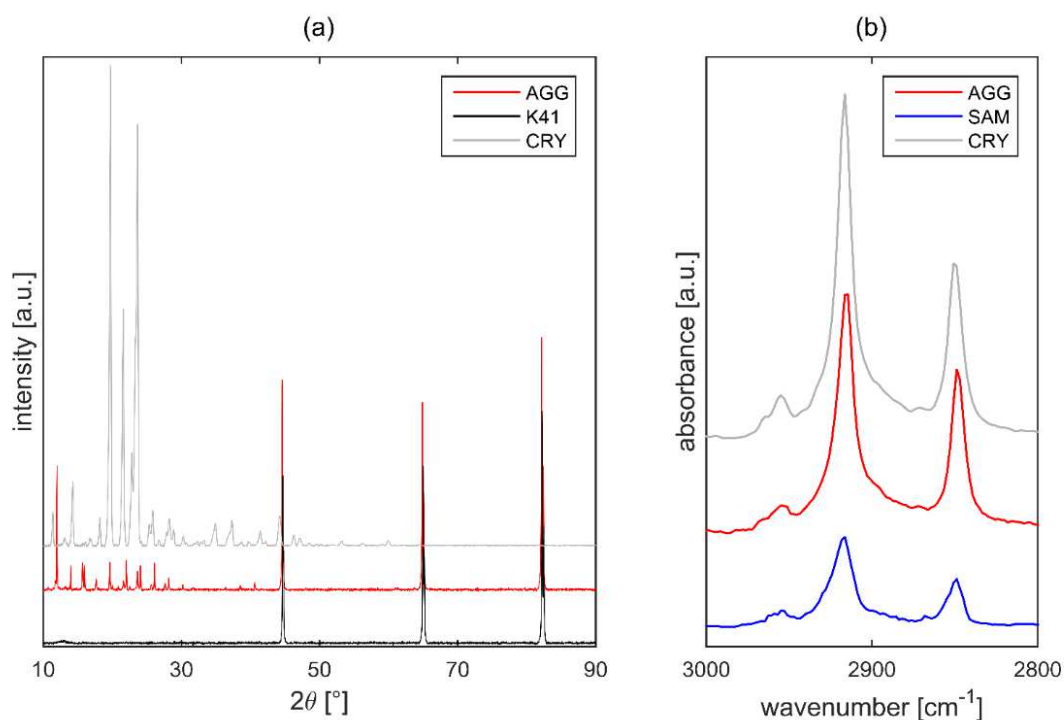


Figure 4: Surface analyses of AGG and SAM samples compared with K41 and CRY used as references. (a) XRD pattern of AGG (red line), K41 (black line), and CRY (light grey line). (b) ATR-FTIR spectra of AGG (red line), SAM (blue line), and CRY (light grey line). For each characterization technique, the intensity scales are the same for the 3 analyses.

Figure 4b shows the ATR-FTIR spectra of SAM, AGG, and CRY samples in the 2800-3000 cm⁻¹ region where the C-H stretching of the methylene group are usually used as references for self-assembled alkyl chains organization^{28,29}. The three samples exhibit extremely similar position of the two main bands appearing in Figure 4b, which are related to the asymmetric and symmetric stretching vibrations of CH₂, $\nu_{as}CH_2$ and ν_sCH_2 respectively. Above all, this confirms the presence of hexadecylphosphonic acids on the surface of AGG and SAM. For the 3 samples, $\nu_{as}CH_2 = 2916$ cm⁻¹ and $\nu_sCH_2 = 2849$ cm⁻¹. These values are consistent with well-organised molecules^{30,31}, since $\nu_{as}CH_2$ values ranging from 2914-2918 cm⁻¹ were reported for crystalline alkane³² characterised by a high degree of order. These results confirms that SAM sample corresponds to a well-organised monolayer. As compared with AGG and CRY, the broadening and lower intensity of the bands for the SAM sample might be notwithstanding attributed to less packed alkyl chains³³. While less pronounced, the bands corresponding to the stretching vibrations of CH₃ at 2955 and 2870 cm⁻¹ also confirm the good organisation of the molecules. It is noteworthy that extremely similar values were reported when functionalising copper¹⁶ or stainless steel³⁴ with the same molecules.

3.2. Tribological performance of AGG

Figure 5 summarizes the results obtained consecutively to the friction tests performed in the framework of the first test campaign, i.e. when 250 friction cycles were achieved with the AGG, SAM and K41 samples. In each graph displayed in Figure 5 referring to different contact pressures, solid lines are the mean of different single tests (6 for AGG and 3 for SAM and K41) which are plotted with dotted lines. Results show a very good reproducibility of the tests in every contact conditions, including for AGG despite the heterogeneous distribution of crystalline aggregates on the surface.

Whatever the contact pressure applied, the friction coefficient (μ) of the un-functionalised sample (K41) is close to 0.2 at the beginning of the test and then suddenly increases to reach a steady-state value close to 0.9. This frictional variation supports an unsurprisingly occurrence of seizure without functionalising stainless steel, due to contact pressures exceeding the yield strength of the material (cf Table 1). Such tribological mechanism is confirmed with SEM observations of the friction tracks displayed in Figures 6c–e where seizure spots and material transfer are clearly visible. It is noteworthy that the higher P_{mean} is, the more pronounced adhesion-transfer related damages are and the wider the friction track is. Analyses of the counterpart's track in Figures 6a and 6b also confirm seizure of the contact through a mixing of adhesion/rough-abrasion scars and the transfer of the ball material onto the K41 plate as the main wearing process involved. **It is worth mentioning that such primary wear mechanism is quiet unconventional since the hardness and the yield strength of the ball are higher than those of the plate (see Table 1).**

Figure 5:

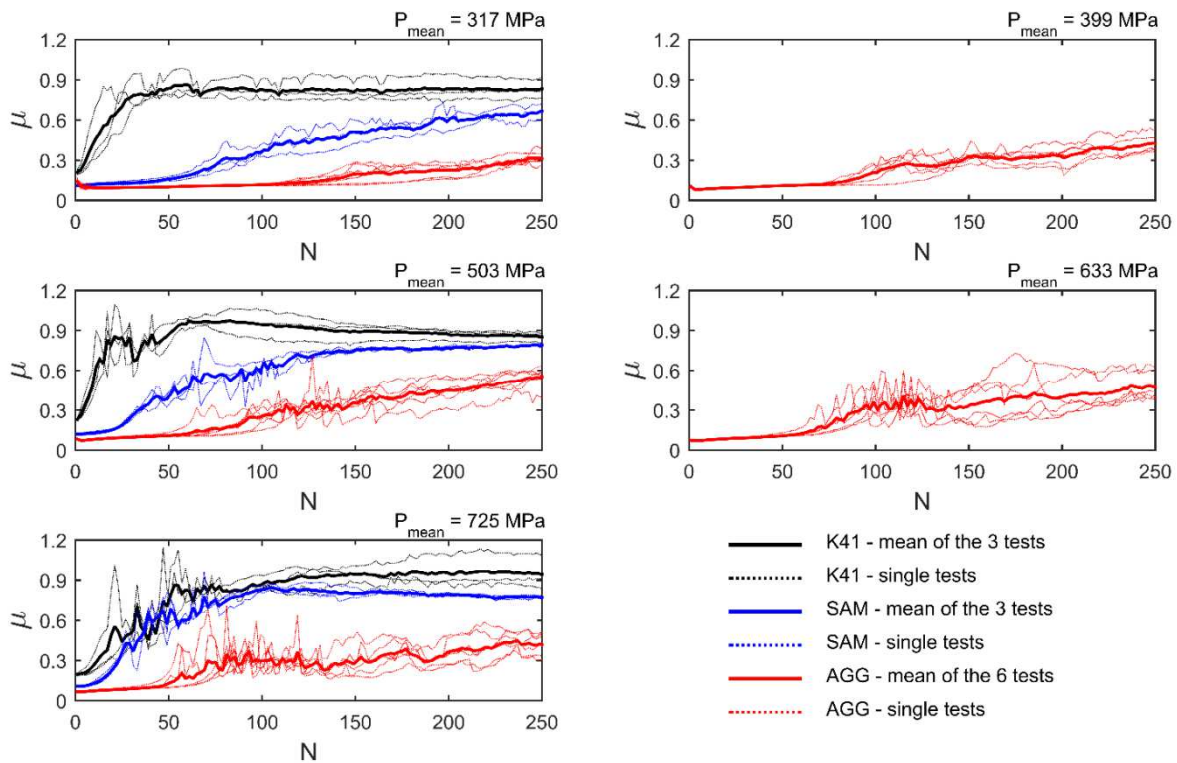


Figure 5: Friction coefficient versus the number of friction cycles (N) when a 100Cr6 ball rubs on K41 (black lines), SAM (blue lines) or AGG (red lines) under $P_{\text{mean}} = 317, 399, 503, 633,$ and 725 MPa. Solid lines refer to the mean of different tests which are plotted with dotted lines.

Functionalising stainless steel with hexadecylphosphonic acids monolayer (SAM samples) leads to an improvement of the frictional behaviour. Disregarding the contact pressure applied, μ is close to 0.11 at the beginning of the test and remains low (inferior to 0.2) throughout a certain amount of friction cycles. Similar friction coefficient values were reported in the literature when immersing the same material²² or copper¹⁵ into a SOL-like liquid containing alkylphosphonic acids. The low-friction stage shows a very small increase of μ versus N ranging from 0.7×10^{-3} to 1.6×10^{-3} per friction cycle. Moreover, very high reproducibility of the frictional behaviour can be pointed out during this stage. Nonetheless, low-friction is no longer ensures after a limited number of friction cycles, which gets smaller and smaller when P_{mean} increases. Afterwards, μ increases towards high values and reaches approximately 0.75 at the end of tests, indicating that seizure occurs similarly to the un-functionalised substrate. Compared with K41, the moderate increase of μ under low contact pressure might be attributed to hexadecylphosphonic molecules still present inside the contact despite an overall gripping state has been reached. Although not presented herein, SEM observations of the friction tracks revealed indeed similar damages than those presented in Figure 6, confirming the limited effect of the monolayer after the completion of some tens of friction cycle.

Figure 6:

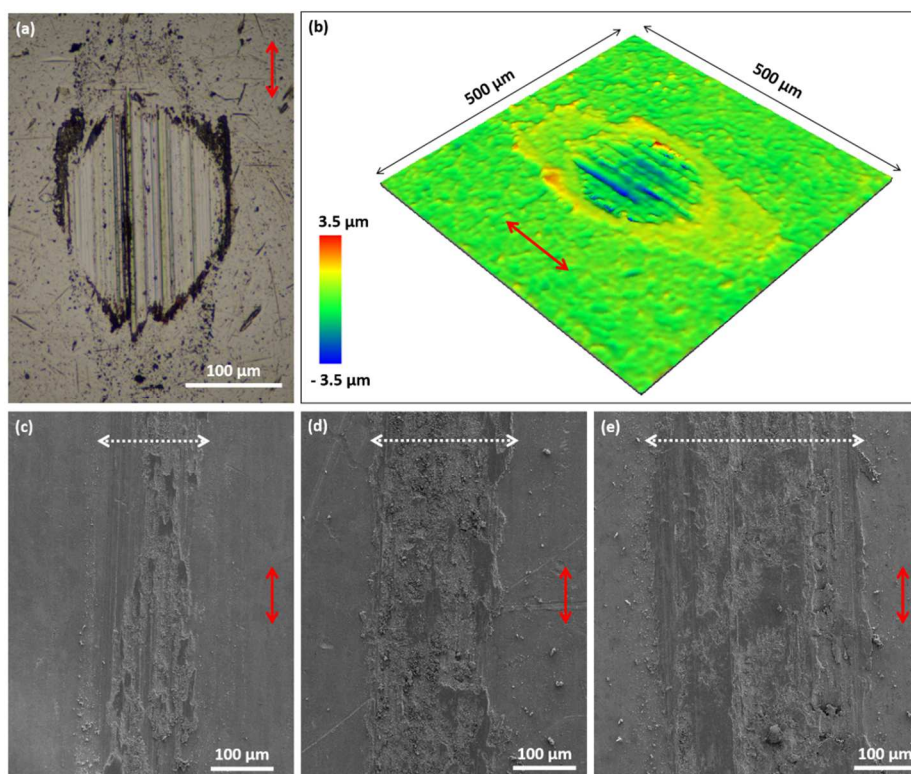


Figure 6: Damages related to the friction tests performed on K41 samples after 250 friction cycles. (a) Microscope observation and (b) surface topography of the same 100Cr6 ball under $P_{\text{mean}} = 503$ MPa. (c, d, e) SEM observations of the plates' friction track under $P_{\text{mean}} = 317$ MPa (c), 503 MPa (d), and 725 MPa (e). Red arrows indicate the friction motion direction and white dotted arrows designate approximately the location and width of the friction track.

To the contrary, the addition of crystalline aggregates of hexadecylphosphonic acid into the contact (AGG) shows a significant improvement of the tribological behaviour. The corresponding red curves in Figure 5 show that lower friction coefficients (close to 0.075) were obtained at the beginning of the test as compared to SAM, except when $P_{\text{mean}} = 317$ MPa. Moreover, an even more stable low-friction stage is observed since the slight increase of μ versus N ranges from 2.9×10^{-4} to 8.4×10^{-4} per friction

cycle, depending on the contact pressure considered. Interestingly, the duration of the low-friction stage strongly increases whatever the contact pressure applied. Moreover, the increase of μ consecutive to this stage appears limited. After 250 friction cycles, the friction coefficient ranges from 0.3 to 0.6 depending on P_{mean} . Figures 7d, 7e and 7f show SEM observations of the friction track after tests performed on AGG under 317, 503 and 725 MPa contact pressure, respectively. Previously physisorbed crystalline platelets of hexadecylphosphonic appear in dark grey in these figures. Obviously, frictional damages are strongly reduced as compared with those related to the unfunctionalised sample, presented in Figure 6. Material transfer does not cover the full track, especially under low pressure, and tracks are less than half as wide. In the outer vicinity of the tracks, cracking and flaking of crystalline platelets has visibly occurred. It is also supposed that some platelet debris should be thereafter trapped inside the contact, since pressed and sheared films originating from these debris appear in the outer border of the tracks.

Figure 7:

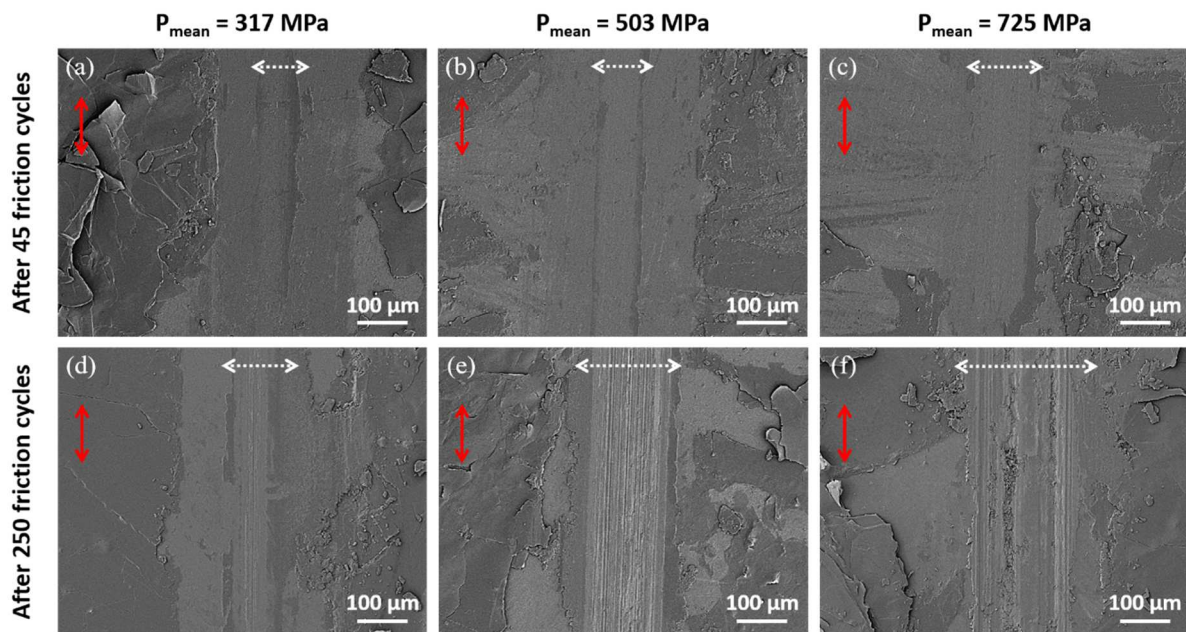


Figure 7: SEM observations at the same magnification of the friction track of AGG samples after 45 (a, b, c) and 250 (d, e, f) friction cycles, under $P_{\text{mean}} = 317$ MPa (a, d), 503 MPa (b, e), and 725 MPa (c, f). Red arrows indicate the friction motion direction and white dotted arrows designate the approximate location and width of the friction track.

When looking at the AGG friction tests results (red curves in Figure 5), it is noteworthy that the low-friction stage remains effective up to approximately 50 friction cycles whatever P_{mean} . Friction tests were consequently stopped after only 45 friction cycles in the framework of a second test campaign. SEM observations of the resulted friction tracks are displayed in Figures 7a-c. All friction tracks exhibit very few damages and the presence of dark films originating from the spreading of platelets' debris, including under high contact pressure.

Typical roughness profiles plotted in a direction perpendicular to friction tracks are presented in Figure 8. These results clearly confirm that strong adhesion and material transfer from the ball to the plate occurred even from the very beginning of the tests performed with K41 samples (grey profiles measured after 45 friction cycles). Conversely, black-plotted profiles related to AGG samples show limited modification of the initial surface roughness after performing 250 friction cycles. Even more interestingly, surface roughness remains unchanged when maintaining the contact in the low-friction stage, except under the highest contact pressure where local adhesion seems to initiate.

Figure 8:

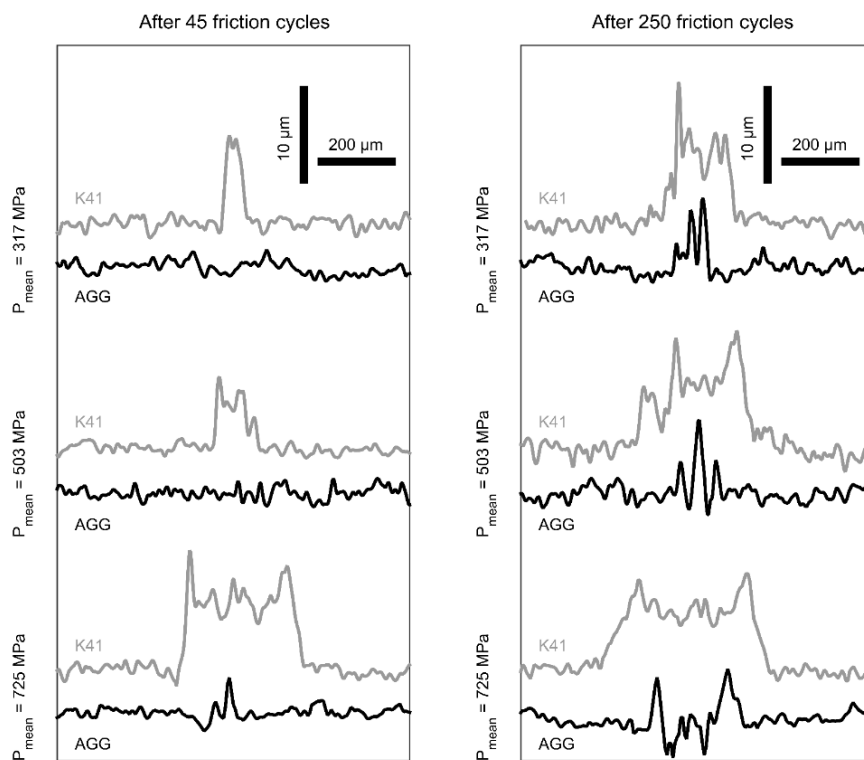


Figure 8: Surface profiles typically measured on K41 (grey line) and AGG (black line) after 45 (left) and 250 (right) friction cycles performed under $P_{\text{mean}} = 317 \text{ MPa}$ (top), 503 MPa (middle), and 725 MPa (bottom). Friction tracks are approximately centred along the roughness profiles.

Tribofilm originating from crystalline aggregates of hexadecylphosphonic might be a relevant explanation of both low-friction and low-wear behaviour observed on AGG samples. As such, it is further investigated in the followings.

3.3. Tribofilm formation and disruption

While μ characterises the mean friction coefficient related to an overall friction cycle, F_T/F_N rather corresponds to a descriptor of the localised variations of the friction force along the friction track. Figure 9, where F_T/F_N is plotted with a coloured scale versus both h and N in the case of AGG sample under $P_{\text{mean}} = 503 \text{ MPa}$, shows a typical example of such variations. It is found that the friction force

remains extremely stable throughout the friction track, especially during the low-friction stage (where $N < 100$). Interestingly, the stability of F_T/F_N is already observed in the very first friction cycles. This supports the extremely fast establishment of an interface procuring favourable tribological behaviour. It seems appropriate in a first instance to attribute this behaviour to a tribofilm originating from hexadecylphosphonic crystalline platelets. Once again, the transition from the low-friction stage to the onset of seizure (N close to 100) shows a remarkable stability along the track. This observation, also coupled with the slight increase of μ during the low-friction stage, underlies a gradual and un-localised disintegration of the film throughout the entire friction track. It is worth mentioning that this behaviour differs from the one observed by Moine *et al* in the case of tribofilm originating from significantly smaller aggregates physisorbed on copper¹⁶, where micro-seizure spots led gradually to widespread seizure.

Figure 9:

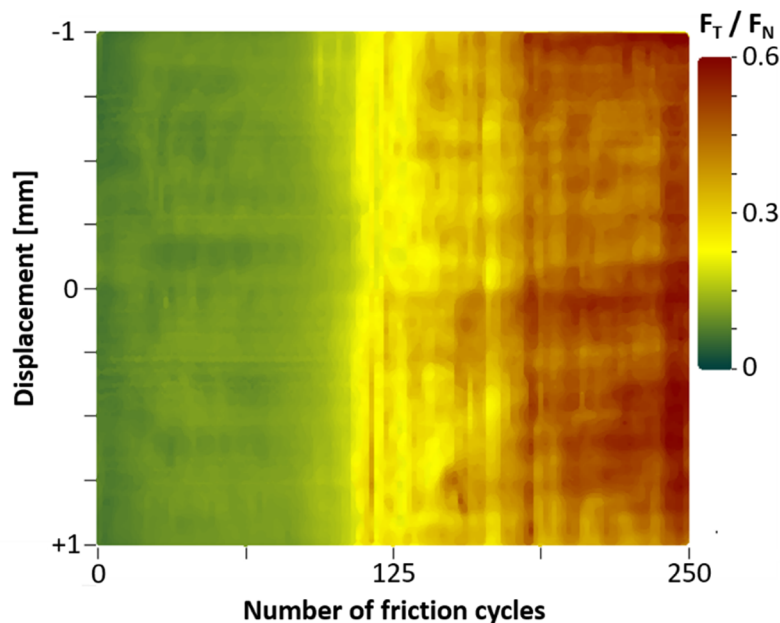


Figure 9: Triboscopic chart showing the evolution of the local friction coefficient F_T/F_N (coloured scale) against the number of friction cycles (abscissa axis) and along the friction track (ordinate axis). Test was performed on AGG under $P_{mean} = 503$ MPa.

Proof of the above-mentioned tribofilm originating from the shearing of crystalline platelets is given in Figure 10. This figure displays SEM observations of both AGG plates and their corresponding counter balls related to friction tests stopped after 1, 3, 11, and 71 friction cycles. Figure 10a demonstrates that a film of sheared crystalline platelets of hexadecylphosphonic was built up over the whole friction track after a single back-and-forth pass. Although not continuous, the film regularly spread over a large part of the track. Interestingly, the associated counter body was highly covered by deformed and fragmented platelets debris originating from the plate (see Figure 10b). Morphology of the film observed on both the plate and the ball shows it was initiated by shearing, spreading and flowing of the original crystalline platelets. Fragmentation of platelets in smaller crystalline particles (of the order of 1 μm long) also occurred as depicted in the Figure 10d inset. After few friction passes, surface coverage of the film quickly decreased, especially in the centre of the plate track (see Figures 10c and 10f). However, some film patches remained inside the contact (see Figure 10e) and their flowing had a healing effect on the fine abrasion ridges generated by harder un-covered asperities from the counterpart (see the Figure 10f inset). Finally, when approaching the onset of the moderate seizure

stage (see Figure 10i), the film was mostly destroyed due to a fine abrasion process, as supported by the Figure 10g inset showing ridges oriented parallel to the friction direction. Figure 10h also suggests the destruction of the film through micro-flaking. SEM observations are also consistent with the above-mentioned interpretations of Figure 9 supporting the homogeneous modification of the interface throughout the friction track.

Figure 10:

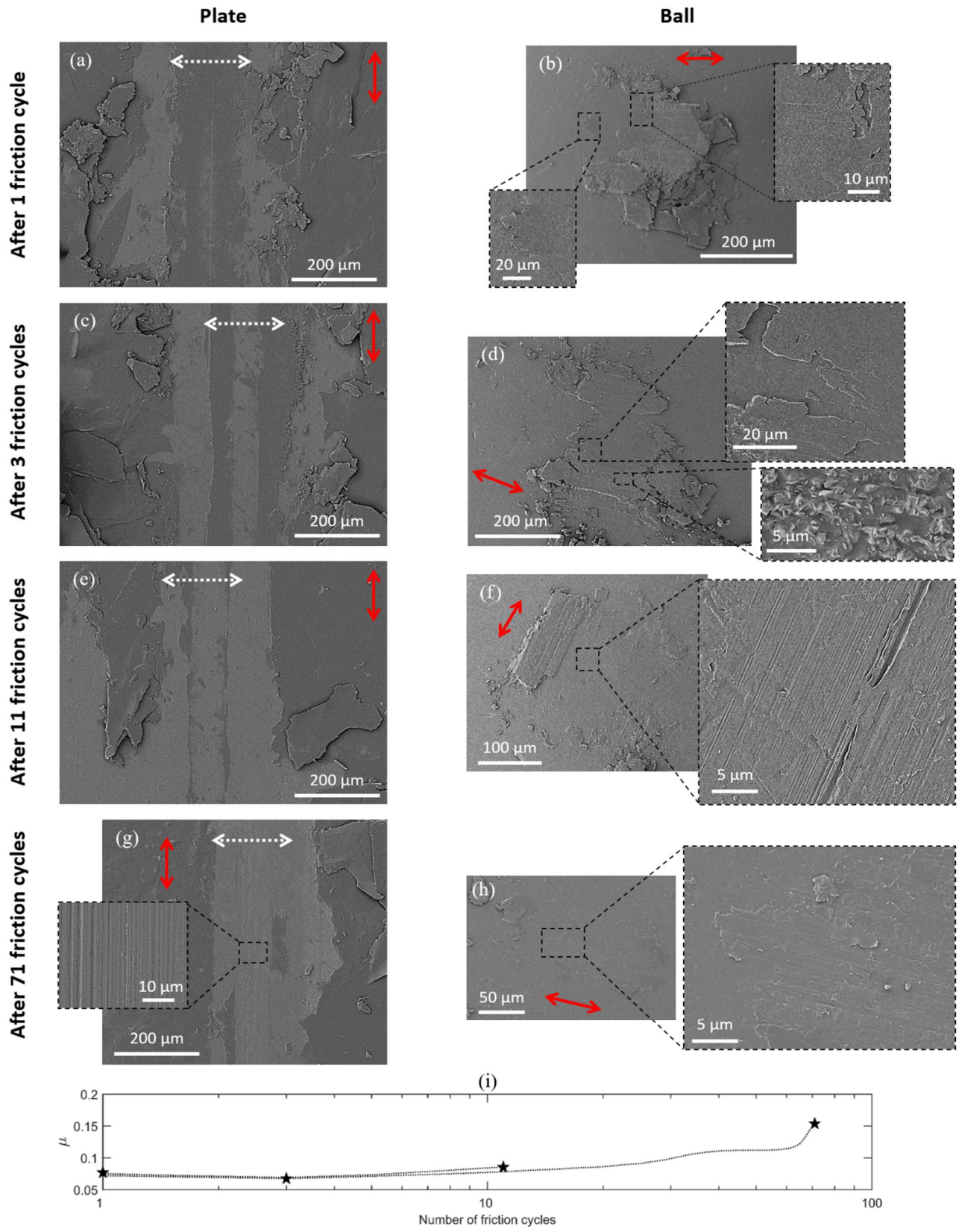


Figure 10: SEM observations of the friction tracks on AGG plates (a, c, e, g) and on the counter balls associated (b, d, f, h) after 1, 3, 11, and 71 friction cycles. Tests were all performed under $P_{mean} = 503$ MPa. Red arrows indicate the friction motion direction and white dotted arrows designate the approximate location and width of the friction track. (i) Evolution of the coefficient of friction corresponding to the 4 contact pairs observed. Stars indicate the end of each test.

3.4. Tribofilm shearing properties

Further interpretations of the friction tests performed with AGG may be addressed to examine the contact pressure dependence of the tribofilm behaviour. With respect to the 5 contact pressures applied, comparison of the mean evolution of μ during the 25 first friction cycles and during the 225 following ones are presented in Figures 11a and 11b, respectively. Figure 11b shows that similar μ were obtained at the end of the low-friction stage. However, the onset of tribofilm breakdown occurred after a number a friction cycles which gets higher and higher when decreasing P_{mean} . Defining N_{onset} as the first friction cycle for which μ exceeds 0.2 leads to Figure 11c showing the significant drop and then the slight decrease of N_{onset} versus P_{mean} . However, it is noteworthy that the lubricated action of the tribofilm remains after approximately 50 cycles (i.e. 20 cm sliding distance) even applying a maximal Hertzian pressure P_{max} as high as 1.1 GPa. Results are compared with the SAM ones, showing the net improvement procured by crystalline aggregates to prolong the low-friction stage whatever P_{mean} .

Figure 11:

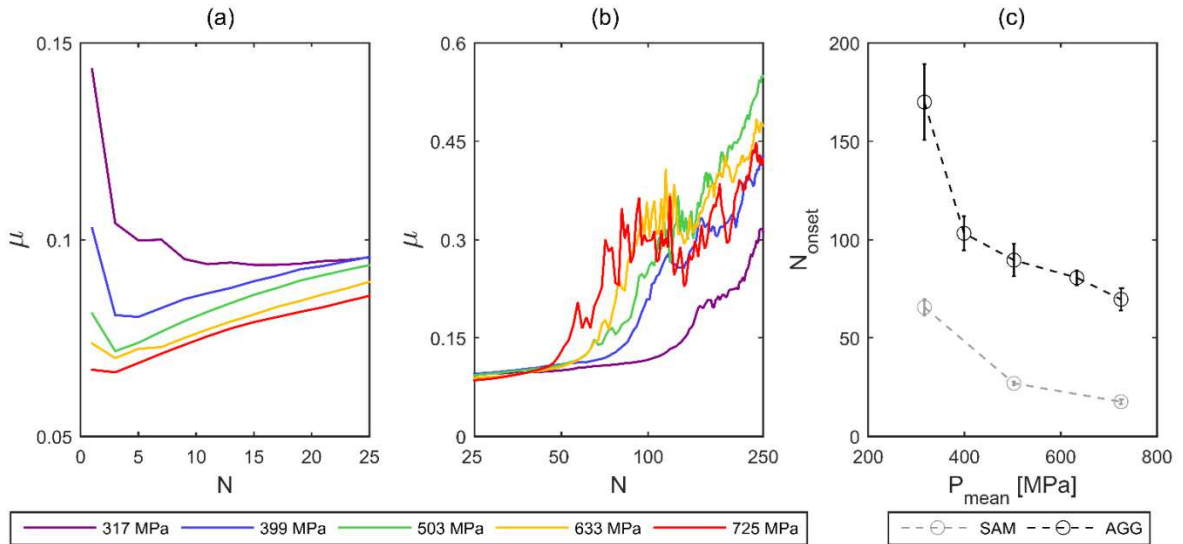


Figure 11: Contact pressure dependence on the evolution of the friction coefficient measured on AGG. (a, b) Evolution of μ versus the number of friction cycles N : during the 25 first friction cycles (a) and during the following 225 friction cycles (b), when P_{mean} ranges from 317 to 725 MPa. Each data point is the mean value originating from 6 different tests. (c) Mean value and standard deviation of the number of friction cycles recovered before the onset of seizure (N_{onset}) versus P_{mean} for AGG sample (black line) as compared with SAM sample (dotted grey line). N_{onset} is defined as the first friction cycle number for which μ exceeds 0.2.

Whereas μ was less dependent on P_{mean} throughout the end of the low-friction stage, significant differences occurred during the 25 first friction cycles, as displayed in Figure 11a. For every contact conditions, μ first decreases and then follows its above-mentioned slight increase. The initial decrease of μ is however significantly lowered when P_{mean} increases and may be attributed to the tribofilm building up. This behaviour should thus reflect a modification of accommodation mechanisms at the very beginning of friction. Since no wear was detected during the 25 first friction cycles, it is assumed that both friction and normal loads applied on the Hertzian area of contact (A) defined as:

$$A = \pi a^2 = \pi \left(\frac{3 F_N R}{2 E^*} \right)^{2/3} \quad (3)$$

where a is the contact radius. Hence, the shear stress (τ) in the contact is:

$$\tau = \frac{F_T}{A} = \frac{F_T}{\pi} \left(\frac{2 E^*}{3 F_N R} \right)^{2/3} \quad (4)$$

The three graphs presented on the left of Figure 12 display the mean value of τ versus P_{mean} for 3 distinctive friction cycles, i.e. the 1st, the 5th, and the 15th ones. Plotting τ versus P_{max} gives of course similar trends. Very different frictional behaviours are observed. For the first friction cycle, the shear stress is close to be independent of the contact pressure. After only 5 friction cycles, τ is linearly correlated with P_{mean} but does not intersect the origin of the graph. This relationship corresponds to the modified Coulomb law which suggests the addition of an adhesive component to the friction force. However, when $N = 15$, the linear trend of τ vs. P_{mean} pass through 0, leading in a very classical behaviour in accordance with the Amontons' laws.

Figure 12:

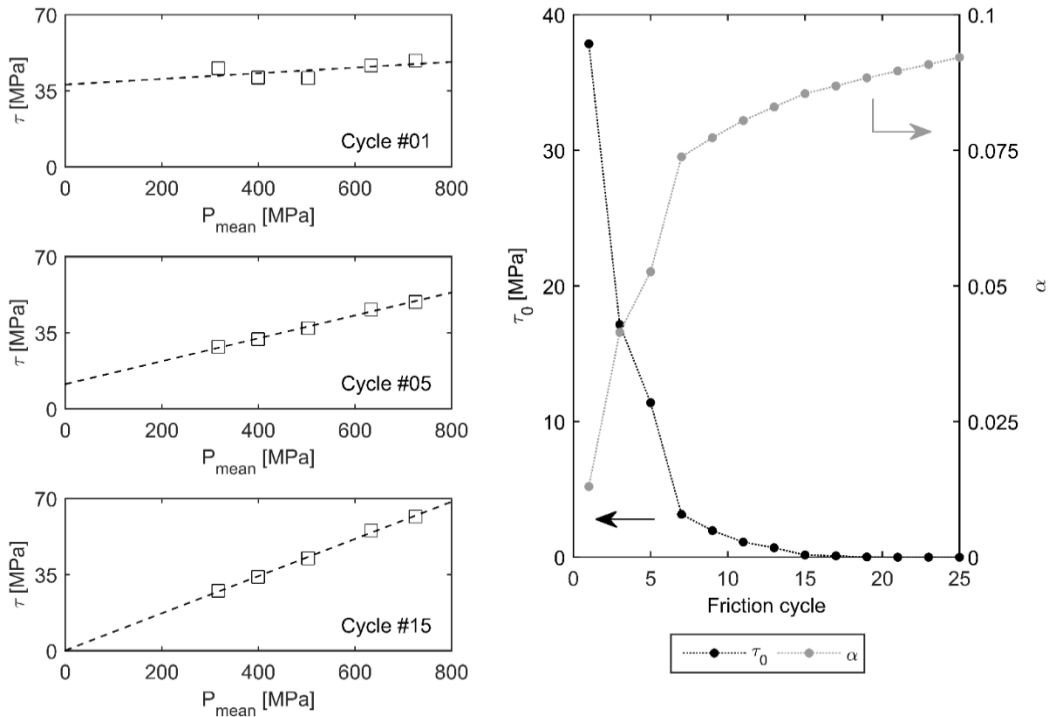


Figure 12: (left) Mean values of shear stress (τ) against P_{mean} related to the 1st, 5th, and 15th friction cycles for the 30 friction tests performed on AGG. Dotted lines are linear regressions. (right) Evolution of the intrinsic shear stress (τ_0) and of the pressure-dependent coefficient (α) during the 25 first friction cycles.

For each friction cycle, the τ vs. P_{mean} trend can be approximated through a linear regression exhibiting Pearson's correlation coefficient $r > 0.98$ in all cases, except for the 1st friction cycle where $r = 0.61$. As composed of hydrocarbonated species, it appears relevant to associate the frictional behaviour of the tribofilm with the one of a polymeric film. According to the excellent works of Briscoe and Tabor in this field³⁵⁻³⁷ and consistently to our experimental observations, it makes sense to write:

$$\tau = \tau_0 + \alpha P_{\text{mean}} \quad (5)$$

where τ_0 is an intrinsic shear stress (not depending on the pressure), and α is a pressure-dependent coefficient. The graph to the right of Figure 12 shows the evolution of τ_0 and α that were calculated for

each friction cycle until $N = 25$. Results highlight the gradual transition of behaviour operated at the beginning of friction. The spreading of crystalline aggregates over the friction track during the first pass is associated to a fixed shear stress that is almost not dependent on the contact pressure ($\tau_0 \neq 0$ and $\alpha \rightarrow 0$). The few following friction cycles, corresponding to the shearing of the tribofilm patches trapped inside the contact, are characterized by the involvement of an adhesive component in the friction force ($\tau_0 \neq 0$ and $\alpha \neq 0$) that quickly decreases. Then, the gradual destruction of the tribofilm leads to a more classical behaviour traditionally observed in dry contacts ($\tau_0 = 0$ and $\alpha = \mu$).

4. Conclusions

This study aims at highlighting the tribological properties conferred by a newly developed surface functionalisation technique based on the adsorption of hexadecylphosphonic acids on the surface of a ferritic stainless steel. The main findings and their related implications in the field of metal forming are listed below.

- (1) After immersion of a ferritic stainless steel in a weakly concentrated solution of hexadecylphosphonic acid, molecular aggregates physisorbed on a well-organised chemisorbed layer were very quickly formed during solvent evaporation without any external operating intervention. These aggregates present a crystalline structure and are mainly in the form of platelets oriented parallel to the surface although three-dimensional clustering of both platelets and needle-shaped crystals occurs. By avoiding operations related to the removal of physisorbed species, this new functionalisation route facilitates surface preparation for subsequent metal forming operation.
- (2) An excellent tribological behaviour of this new functionalisation were observed under relevant contact conditions regarding metal forming operations. Seizure was completely prevented over sliding distances in the order of several hundreds of millimetres that are suitable for many metal forming operations, even under maximal contact pressure exceeding 1 GPa. No wear and almost no modification of surface roughness were detected.
- (3) Friction was considerably reduced through this functionalisation technique. Friction coefficients lower than 0.1 and exhibiting high stability both over time and along the friction track were measured. As compared to the chemisorbed layer alone (SAM), the presence of aggregates decreased by approximately 25% the friction coefficient and increased by more than 200% the duration of the low-friction stage. Consequently, energy consumption reduction and higher length of deformation in metal forming operations are expected.
- (4) Low-wear and low-friction is explained by the very fast establishment of a tribofilm over the friction track since the first pass of the counterpart. The tribofilm originates from the shearing of crystalline platelets and is then gradually eliminated through micro-flaking, causing a slight but reasonable increase of the friction coefficient. Unfortunately, results did not provide information on whether the crushing of three-dimensional clusters infer on the tribofilm morphology and behaviour. Interestingly, the tribofilm adheres on the two surfaces of the contact pair, meaning that both the tool and the metal sheet could be efficiently protected in the framework of metal forming.
- (5) The shearing mechanism of the tribofilm exhibits an interesting pressure dependency transition during the first millimetres of sliding distance. From a shear stress approximately independent of the pressure, to a classical Amonton-like behaviour, the film exhibits a friction law containing an adhesive term which decreases versus the sliding distance. A direct key consequence is that the friction coefficient gets lower and lower when the contact pressure increases along the first tens of millimetres of sliding distance. This feature should be extremely beneficial in metal forming in order to enhance the maximal permitted mechanical stresses.

Since different aggregates morphologies (size, distribution on the surface, crystal structure...) were observed depending on the material substrate and the evaporation step protocol, further works have to be carried out to investigate their effect on the tribological behaviour. Moreover, investigations at the micro and nano scales are being performed at the moment to characterize the local interaction between a single counterpart asperity and crystalline aggregates.

Acknowledgments

The authors wish to sincerely thank Mélanie Borgeot for XRD measurements, Aurélien Buteri from APERAM Inc. for the supply of stainless steel samples, Luc Carpentier for data acquisition software and topographic images post-treatment software programming, Nicolas Rouge for SEM images, Vincent Tissot for machining sample holders, and Guillaume Colas for critical comments on the original manuscript. This work was supported by the EIPHI Graduate School (contract ANR-17-EURE-0002).

References

1. Andreasen, J. L., Bay, N., Andersen, M., Christensen, E. & Bjerrum, N. Screening the performance of lubricants for the ironing of stainless steel with a strip reduction test. *Wear* **207**, 1–5 (1997).
2. Bay, N., Olsson, D. D. & Andreasen, J. L. Lubricant test methods for sheet metal forming. *Tribol. Int.* **41**, 844–853 (2008).
3. Vollertsen, F. & Schmidt, F. Dry metal forming: Definition, chances and challenges. *Int. J. Precis. Eng. Manuf. - Green Technol.* **1**, 59–62 (2014).
4. Huang, W., Tan, Y., Dong, J. & Chen, B. Tribological properties of the film formed by borated dioctyl dithiocarbamate as an additive in liquid paraffin. *Tribol. Int.* **35**, 787–791 (2002).
5. Syahir, A. Z. *et al.* A review on bio-based lubricants and their applications. *J. Clean. Prod.* **168**, 997–1016 (2017).
6. Cortes, V. & Ortega, J. A. Evaluating the Rheological and Tribological Behaviors of Coconut Oil Modified with Nanoparticles as Lubricant Additives. *Lubricants* **7**, 76 (2019).
7. Alves, S. M., Barros, B. S., Trajano, M. F., Ribeiro, K. S. B. & Moura, E. Tribological behavior of vegetable oil-based lubricants with nanoparticles of oxides in boundary lubrication conditions. *Tribol. Int.* **65**, 28–36 (2013).
8. Cheng, H. & Hu, Y. Influence of chain ordering on frictional properties of self-assembled monolayers (SAMs) in nano-lubrication. *Adv. Colloid Interface Sci.* **171–172**, 53–65 (2012).
9. Ulman, A. *An introduction to ultrathin organic films: Langmuir-Blodgett to self-assembly.* (Academic Press, 1991).
10. Ahn, H. S., Cuong, P. D., Park, S., Kim, Y. W. & Lim, J. C. Effect of molecular structure of self-assembled monolayers on their tribological behaviors in nano- and microscales. *Wear* **255**, 819–825 (2003).
11. Patois, T. *et al.* Microtribological and corrosion behaviors of 1H,1H,2H,2H-perfluorodecanethiol self-assembled films on copper surfaces. *Surf. Coatings Technol.* **205**, 2511–2517 (2010).
12. Cichomski, M., Kośła, K., Pawlak, W., Kozłowski, W. & Szmaja, W. Stability and tribological investigations of 1H, 1H, 2H, 2H-perfluoroalkyltrichlorosilane on titania surface. *Tribol. Int.* **77**, 1–6 (2014).
13. Gao, W., Dickinson, L., Grozinger, C., Morin, F. G. & Reven, L. Self-assembled monolayers

- of alkylphosphonic acids on metal oxides. *Langmuir* **12**, 6429–6435 (1996).
14. Wan, Y. *et al.* Enhanced tribology durability of a self-assembled monolayer of alkylphosphonic acid on a textured copper substrate. *Appl. Surf. Sci.* **259**, 147–152 (2012).
 15. Roizard, X. *et al.* Insights into sliding wear and friction behavior of copper in ethanol containing alkylphosphonic acid molecules. *Tribol. Int.* **96**, 141–148 (2016).
 16. Moine, M. M. *et al.* Grafting and characterization of dodecylphosphonic acid on copper: Macro-tribological behavior and surface properties. *Surf. Coatings Technol.* **232**, (2013).
 17. Brukman, M. J., Marco, G. O., Dunbar, T. D., Boardman, L. D. & Carpick, R. W. Nanotribological properties of alkanephosphonic acid self-assembled monolayers on aluminum oxide: Effects of fluorination and substrate crystallinity. *Langmuir* **22**, 3988–3998 (2006).
 18. Cichomski, M., Kośła, K., Grobelny, J., Kozłowski, W. & Szmaja, W. Tribological and stability investigations of alkylphosphonic acids on alumina surface. *Appl. Surf. Sci.* **273**, 570–577 (2013).
 19. Zhang, C. X., Liu, Y. H. & Wen, S. Z. Excellent tribological behavior of hexadecylphosphonic acid films formed on titanium alloy. *Sci. China Technol. Sci.* **57**, 1816–1823 (2014).
 20. Cichomski, M. *et al.* Tribological and corrosive investigations of perfluoro and alkylphosphonic self-assembled monolayers on Ti incorporated carbon coatings. *Tribol. Int.* **130**, 359–365 (2019).
 21. Hill, D. *et al.* Study of the tribological properties and ageing of alkylphosphonic acid films on galvanized steel. *Tribol. Int.* **119**, 337–344 (2018).
 22. Roizard, X. *et al.* Friction behavior of ferritic stainless steel in a strongly diluted alcohol solution of alkylphosphonic acid. *Tribol. Int.* **118**, 465–473 (2018).
 23. Lallemand, F., Roizard, X., Melot, J. M., Buteri, A. & Borgeot, M. Wo 2016/046401. (2016).
 24. Buteri, A. *et al.* Tribological behavior of a new green industrial lubricant for stamping operations - Application to Stainless Steels. *IOP Conf. Ser. Mater. Sci. Eng.* **159**, (2016).
 25. Verma, R. K. & Chandra, S. An improved model for predicting limiting drawing ratio. *J. Mater. Process. Technol.* **172**, 218–224 (2006).
 26. Cornuault, P.-H., Colas, G., Lenain, A., Daudin, R. & Gravier, S. On the diversity of accommodation mechanisms in the tribology of Bulk Metallic Glasses. *Tribol. Int.* **141**, (2020).
 27. Gao, W., Dickinson, L., Morin, F. G. & Reven, L. Phase Transitions in Lamellar Alkylphosphonate Salts. *Chem. Mater.* **9**, 3113–3120 (1997).
 28. Snyder, R. G., Strauss, H. L. & Elliger, C. A. C-H stretching modes and the structure of n-alkyl chains. 1. Long, disordered chains. *J. Phys. Chem.* **86**, 5145–5150 (1982).
 29. MacPhail, R. A., Strauss, H. L., Snyder, R. G. & Elliger, C. A. C-H stretching modes and the structure of n-alkyl chains. 2. Long, all-trans chains. *J. Phys. Chem.* **88**, 334–341 (1984).
 30. Bhure, R., Abdel-Fattah, T. M., Bonner, C., Hall, J. C. & Mahapatro, A. Formation of nanosized phosphonic acid self assembled monolayers on cobalt-chromium alloy for potential biomedical applications. *J. Biomed. Nanotechnol.* **6**, 117–128 (2010).
 31. Van Alsten, J. G. Self-assembled monolayers on engineering metals: Structure, derivatization, and utility. *Langmuir* **15**, 7605–7614 (1999).
 32. Quiñones, R., Raman, A. & Gawalt, E. S. Functionalization of nickel oxide using alkylphosphonic acid self-assembled monolayers. *Thin Solid Films* **516**, 8774–8781 (2008).
 33. Yee, C. *et al.* Self-assembled monolayers of alkanesulfonic and -phosphonic acids on amorphous iron oxide nanoparticles. *Langmuir* **15**, 7111–7115 (1999).
 34. Raman, A., Dubey, M., Gouzman, I. & Gawalt, E. S. Formation of self-assembled monolayers

- of alkylphosphonic acid on the native oxide surface of SS316L. *Langmuir* **22**, 6469–6472 (2006).
35. Amuzu, J. K. A., Briscoe, B. J. & Tabor, D. Friction and shear strength of polymers. *ASLE Trans.* **20**, 354–358 (1977).
 36. Briscoe, B. J. & Tabor, D. The Effect of Pressure on the Frictional Properties of Polymers. *Wear* **34**, 29–38 (1975).
 37. Briscoe, B. J. & Tabor, D. Shear Properties of Thin Polymeric Films. *J. Adhes.* **9**, 145–155 (1978).